JCI insight

RyR$_2$^{R420Q} catecholaminergic polymorphic ventricular tachycardia mutation induces bradycardia by disturbing the coupled clock pacemaker mechanism

Yue Yi Wang,[1] Pietro Mesirca,[2] Elena Marqués-Sulé,[1,3] Alexandra Zahradnikova Jr.,[1] Olivier Villejoubert,[1] Pilar D'Ocon,[4] Cristina Ruiz,[5] Diana Domingo,[6] Esther Zorio,[6] Matteo E. Mangoni,[2] Jean-Pierre Benitah,[1] and Ana María Gómez[1]

[1]UMR-S 1180, Inserm, Université Paris-Sud, Université Paris-Saclay, Châtenay-Malabry, France. [2] UMR-5203, CNRS, INSERM U1191, Institut de Génomique Fonctionnelle, Département de Physiologie, Université de Montpellier, Montpellier, France. [3]Physiotherapy Department, [4]ERI BIOTECMED and Department of Pharmacology School, University of Valencia, Valencia, Spain. [5]Radiodiagnostic and [6]Cardiology Department, Hospital Universitario y Politécnico La Fe, Valencia, Spain.

Catecholaminergic polymorphic ventricular tachycardia (CPVT) is a lethal genetic arrhythmia that manifests syncope or sudden death in children and young adults under stress conditions. CPVT patients often present bradycardia and sino-atrial node (SAN) dysfunction. However, the mechanism remains unclear. We analyzed SAN function in two CPVT families and in a novel knock-in (KI) mouse model carrying the RyR$_2$^{R420Q} mutation. Humans and KI mice presented slower resting heart rate. Accordingly, the rate of spontaneous intracellular Ca^{2+} ([Ca^{2+}]$_i$) transients was slower in KI mouse SAN preparations than in WT, without any significant alteration in the "funny" current (I_f). The L-type Ca^{2+} current was reduced in KI SAN cells in a [Ca^{2+}]$_i$-dependent way, suggesting that bradycardia was due to disrupted crosstalk between the "voltage" and "Ca^{2+}" clock, and the mechanisms of pacemaking was induced by aberrant spontaneous RyR$_2$- dependent Ca^{2+} release. This finding was consistent with a higher Ca^{2+} leak during diastolic periods produced by long-lasting Ca^{2+} sparks in KI SAN cells. Our results uncover a mechanism for the CPVT-causing RyR$_2$ N-terminal mutation R420Q, and they highlight the fact that enhancing the Ca^{2+} clock may slow the heart rhythm by disturbing the coupling between Ca^{2+} and voltage clocks.

Introduction

Catecholaminergic polymorphic ventricular tachycardia (CPVT) is an inherited heart disease manifested with syncope or sudden cardiac death (SCD) in children and young adults under physical or emotional stress (1). Although CPVT stands for ventricular arrhythmia, it often associates supraventricular (SV) arrhythmias, including not only tachyarrythmias (atrial fibrillation and atrial flutter), but also bradyarrythmias such as sinus bradycardia caused by sino-atrial node (SAN) dysfunction (2–4). These findings may be of paramount importance in CPVT carriers with implantable cardioverter defibrillator (ICD) devices, since on the top of the expected β-blocker–induced bradycardia, severe SAN bradycardia dysfunction may prompt them to use their pacing mode, thus reducing the life of their ICD batteries.

Thus, CPVT arrhythmic disorders are not only limited to the ventricles, as CPVT-related mutations are also expressed in the entire heart. Indeed, Postma et al. (2) investigated 13 missense mutations in the cardiac ryanodine receptor (RyR$_2$) in 12 probands and reported that the RyR$_2$ mutation carriers exhibit bradycardia, regardless of the site of the mutation. In keeping with this observation, van der Werf et al. (5) investigated 160 relatives from 15 families, and they observed sinus bradycardia and other SV dysrhythmias in 19% and 16% of relatives, respectively.

The heartbeat is initiated by the automatic electrical firing of the primary pacemaker, located at the SAN. SAN cells automatically generate action potentials (AP), which are then conducted to the atria and ventricles, assuring the coordinated contraction of the heart. The mechanism of the automatic AP generation involves several ionic currents and transporters. While the hyperpolarization activated current "fun-

ny" (I_f) current plays an important role, intracellular Ca^{2+} dynamics is also involved (6, 7). Indeed, it has been proposed that rhythmic sarcoplasmic reticulum (SR) Ca^{2+} release via RyR_2 (Ca^{2+} clock) couples with the activity of sarcolemmal channels such as I_f and L-type Ca^{2+} current (I_{CaL}) (membrane clock) to control SAN automaticity (7, 8). The involvement of RyR_2-dependent Ca^{2+} release in SAN automaticity has been demonstrated in numerous studies showing that addition of ryanodine slowed down SAN pacemaker activity in different species (9–13). In addition, inducible and cardiac-specific KO of RyR_2 with acute ~50% loss of the RyR_2 protein was sufficient to cause bradycardia and arrhythmias (14).

Mutations in at least four genes — RyR_2, calsequestrin (CASQ2), triadin (TRDN), and calmodulin (CALM1) — are known to cause CPVT. Approximately 50%–65% of CPVT identified mutations are autosomal dominant mutations in RyR_2. An impaired β-adrenergic SAN response producing SAN pauses was reported by our group in a RyR_2-related CPVT mouse model carrying the C-terminal $RyR_2{}^{R4496C}$ mutation (15), due to an increased Ca^{2+} sensitivity (16). Of note, mutations in other regions of the RyR_2 protein have not been studied with regard to their SAN proarrhythmic potential. The CPVT RyR_2 mutations are primarily clustered in three discrete regions of the RyR_2 protein, namely the N-terminal (residues 77–466), the central (residues 2,246–2,534), and the C-terminal region (residues 3,778–4,959) (17). Thus, it is possible that the mechanism underlying arrhythmic disorders differs according to the site of the mutation within the protein.

In the present study, we have created a new mouse model of CPVT to study the SAN activity of the knock-in (KI) mice carrying RyR_2 N-terminus $RyR_2{}^{R420Q}$ mutation. This mutation has been previously reported (18–20) and characterized by our group, showing a high prevalence of sinus bradycardia (20). Although CPVT affects equally men and women, for some yet unknown reason, male CPVT patients were reported to exhibit a higher risk of cardiac events and lower resting heart rate (HR) (2, 21). Whether these two features exhibit a cause-effect relationship has not been excluded. Thus, we have separately analyzed $RyR_2{}^{R420Q}$ males and females. Those parameters without differences stratified by sex were pooled together. Other possible mechanisms to explain the presence of sinus bradycardia have been explored in patients with the RyR_2 mutation and nonaffected relatives. A sympathetic denervation, as a possible cause of sinus bradycardia, was not observed in our CPVT patients harboring the $RyR_2{}^{R420Q}$ mutation, since β-adrenoreceptor (β-AR) expression and ^{123}I-MIBG (labeled metaiodobenzylguanidine) cardiac sympathetic scintigraphy imaging reflected normal function. Meanwhile, this N-terminus mutation altered the Ca^{2+} homeostasis of SAN cells in KI mice irrespective of sex. Indeed, $RyR_2{}^{R420Q}$-KI SAN cells showed prolonged Ca^{2+} sparks, with consequent enhanced diastolic Ca^{2+} leak. Rather than accelerating pacemaker activity, Ca^{2+} leak during the diastolic phase partially inactivated I_{CaL}, a phenomenon which is generated by the uncoupled RyR_2-dependent Ca^{2+} release from membrane automaticity. This impairment of the "coupled clock" pacemaker mechanism resulted in slowing of the SAN firing rate.

Results

Human data. We previously showed that sinus bradycardia (sinus rhythm < 60 bpm) was associated with the presence of the $RyR_2{}^{R420Q}$ mutation in humans (20). We now present data on original and additional patients from another apparently unrelated family bearing the same $RyR_2{}^{R420Q}$ mutation, analyzing resting HR as a continuous variable and stratified by sex. Our data (Figure 1A) show that HR was lower in $RyR_2{}^{R420Q}$ carriers than in noncarriers, before any β-blocker therapy was administered.

Besides the intrinsic defect related to the RyR_2 mutation, other mechanisms may account for the observed sinus bradycardia, such as a decreased sympathetic tone due to a lower β-AR density and/or a reduced presynaptic catecholamine recycling. The resulting sympathetic denervation may create a proarrhythmic substrate, which could contribute to the initiation of sustained ventricular arrhythmias (22). In this scenario, a given increase in the systemic autonomic tone may trigger a life-threatening arrhythmia in a denervated hypersensitive myocardium, which may accentuate electric heterogeneities of primary arrhythmic conditions (22).

In order to examine whether the decrease in HR in our CPVT patients was due to remodeling of β-adrenergic signaling, we examined β1 and β2 expression levels, as well as G protein coupled receptor kinase (GRKs), which mediate phosphorylation and internalization of β-AR. Analysis of mRNA levels of β1 and β2 adrenoceptors — and GRK2, GRK3, and GRK5 — were shown to be unaltered (Supplemental Figure 1; supplemental material available online with this article; https://doi.org/10.1172/jci.insight.91872DS1) suggesting that the HR differences are not due to differences in β-AR densities. We further investigated the cardiac sympathetic innervation by analyzing scintigraphic parameters. Both early and late heart-to-mediastinum (H/M) ratios and washout rate (WR) on planar imaging
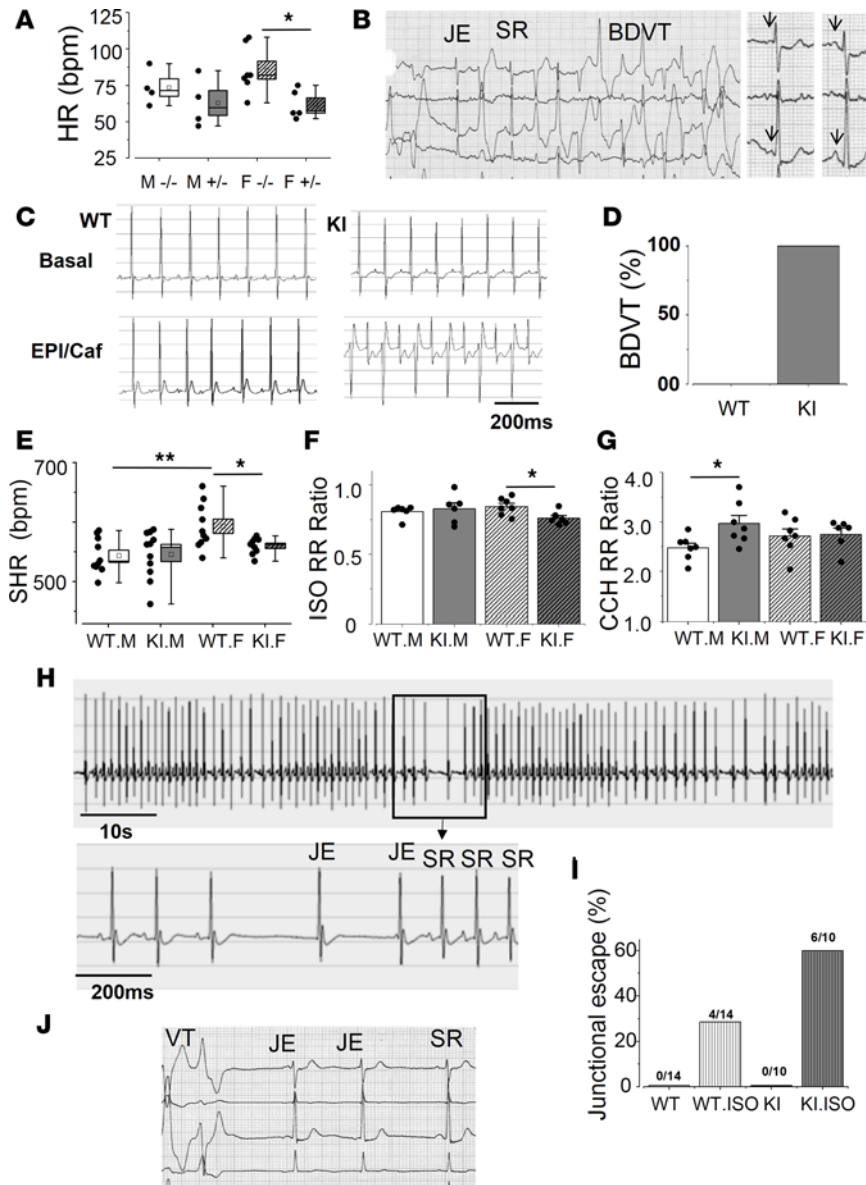
Figure 1. RyR$_2$^{R420Q} CPVT mutation causes sinus dysfunction. (**A**) Heart rate (bpm) of the family members without the mutation (–/–) or heterozygous for the RyR$_2$^{R420Q} mutation (+/–), male (M) and females (F). n = 4 M–/–, 4 M+/–, 7 F–/–, and 5 F+/–. Two-way ANOVA revealed a genotype statistical difference at P = 0.006. (**B**) Recovery of an exercise testing in a 57-year-old female carrier of the RyR$_2$^{R420Q} mutation depicting a junctional escape beat (JE) overcoming a pause caused by a ventricular ectopy and then followed by a burst of bidirectional ventricular tachycardia (BDVT), with a period of sinus rhythm (SR) in between. (**C**) Representative examples of ECG recordings obtained before (top panels) and following (bottom panels) epinephrine (2 mg/Kg) + caffeine (120 mg/Kg) injection (i.p.) in a WT mouse (left) and a KI mouse (right). The KI mouse shows BDVT after epinephrine/caffeine administration, characteristic of CPVT mice. (**D**) After injection, all of the KI mice (n = 7) show BDVT, but none of the WT show BDVT (n = 5). (**E**) Sinus heart rhythm (SHR), calculated from PP intervals recorded during daytime. KI female mice (n = 9) beat slower than WT (n = 10). No difference was found for the males (WT n = 10 vs. KI n = 11). (**F**) Isoproterenol (ISO, 1 mg/kg, i.p.) decreased the RR interval in both WT (male n = 6 and female n = 7) and KI (male n = 6 and female n = 6) mice. The KI females decreased proportionally more than WT. Ratio represents the RR interval after ISO injection normalized by the RR interval in the same animal before ISO injection. (**G**) Carbachol (CCH, 0.25 mg/kg, i.p.) increased the RR intervals in all mice. WT male n = 7, WT female n = 7, KI male n = 7, KI female n = 6. (**H**) ECG example of a KI mouse after ISO injection showing JE overcoming a transient severe decrease in sinus rate. Scale bar: 10 s. Below, a portion of the same ECG is shown. Scale bar: 200 ms. (**I**) Proportion of animals presenting JEs after ISO injection. (**J**) Two JEs during a self-terminating SAN dysfunction period induced by ventricular ectopies during the exercise testing in a 35-year-old female carrier of the RyR$_2$^{R420Q} mutation. For the box and whisker plots, the horizontal line in each box is the median and the square represents the mean, while the box displays the ± SEM and the whiskers extends from minimum to maximum values, with the individual data shown on the left. The bar graph represents the mean ± SEM, with individual data on the bar graph. White bar represents WT and gray bar represents KI, while the diagonal stripes stand for females, and vertical stripes indicate ISO stimulation. *P < 0.05; **P < 0.01 by Student's t test.

with ^{123}I-MIBG remained within normal values, with H/M ≥ 1.6 in all of them, a mean value 1.87 ± 0.14 and a WR mean value 26.125 ± 7.06%. Representative images from one of the patients are given in Supplemental Figure 2. Briefly, these data fail to evidence any difference in the β-AR level or presynaptic innervation in CPVT patients.

Mice model. To understand the mechanism underlying bradycardia and SAN dysfunction in RyR$_2$^{R420Q} patients, we created a KI mouse model carrying RyR$_2$^{R420Q} mutation. We analyzed ECGs in freely moving KI and their WT littermates by telemetry. As exercise in humans (Figure 1B), a pharmacological stress challenge (epinephrine/caffeine injection, 2/120 mg/kg) provoked typical CPVT ventricular arrhythmias in KI mice but not in their WT littermates (Figure 1, C and D), thus validating the model. In the mouse model, ventricular arrhythmia was often sustained, and 100% of the RyR$_2$^{R420Q} mutation–carrying mice exhibited bidirectional ventricular tachycardia (BDVT). In contrast, among the CPVT patients of the human families carrying the same mutation, only one exhibited BDVT. Also, ventricular arrhythmias were always nonsustained, and the remaining ventricular arrhythmic burden comprised polymorphic nonsustained ventricular tachycardia, ventricular couplets, and/or frequent ventricular ectopic activities (20). In order to analyze sinus rhythm, we analyzed sinus heart rhythm (SHR, number of P waves per minute). During activity night-time period, there were no significant differences in SHR between KI and WT mice (males: 579.83 ± 9.06 vs. 586.37 ± 13.05, in 10 WT mice and 11 KI mice, respectively; females: 621.99 ± 17.82 in 10 WT vs. 591.63 ± 10.07 in 9 KI mice). However, during resting day-time period, when the sympathetic tone is reduced, we found a significantly slower SHR in KI females than WT females (Figure 1E), reminiscent of human data (Figure 1A). Additionally, we found that WT female mice exhibit faster SHR than WT males (Figure 1E), reminiscent of human data (Figure 1A).

Sympathetic and parasympathetic responses of the RyR$_2$^{R420Q} mice. In order to analyze the SAN response, we challenged RyR$_2$^{R420Q} mice with two opposite approaches: activation of either the sympathetic (isoproterenol [ISO], i.p. injection, 1 mg/kg) or the parasympathetic (carbachol [CCH], i.p. injection, 0.25 mg/kg) nervous system. As data on RR intervals were similar to data on PP intervals, from here on out, we only report on RR intervals, which are easier to identify (Figure 1E and Supplemental Figure 3).

As expected, ISO had a positive chronotropic effect (Figure 1F), and CCH had a negative chronotropic effect (Figure 1G) in all mice. Comparison between WT and KI mice, in sex, showed a stronger ratio effect of ISO in KI females than in WT females (Figure 1F) and of CCH in KI males than in WT males (Figure 1G). The higher ISO effect in HR in KI females (which had lower basal HR than WT in basal conditions) erased the genotype differences. Thus, following ISO injection, there were no differences in HR among groups (Supplemental Figure 3).

Remarkably, RyR$_2$^{R420Q}-KI mice also presented signs of SAN dysfunction after ISO injection, notably evidenced by a variable decrease in the SHR followed by the appearance of junctional escapes (JEs) (Figure 1, H and I). Since no sex difference was observed, data were pooled together. Stress-triggered JEs were also present in RyR$_2$^{R420Q} humans (Figure 1, B and J).

We then explored another arrhythmia trigger, emotional stress, by blowing the mice with warm air from a hair-dryer during 15 seconds followed by 45 seconds of rest, and repeated up to 10 times (23). The RR intervals of a WT and a KI mouse are shown during this protocol in Figure 2A. Each time while the air is blown, the HR accelerated and then recovered during the resting periods. At the end of the protocol, the KI mouse developed severe SAN dysfunction (Figure 2A, bottom) with a slow ventricular escape rhythm until asystole occurred and the mouse died. Most of the KI mice (5 of 7) died after this protocol. Figure 2B shows the percentage of mice presenting ventricular escape rhythm before and after the protocol. Figure 2C is the ECG recording of a KI mouse, which died during the recovery phase. Strikingly, stress-induced ventricular tachycardia (VT) (manifested as shortened RR intervals; Figure 2A, bottom) were self-terminated, and the final arrhythmia underlying the SCD 3 hours later was a bradyarrhythmia, namely a severe SAN dysfunction with a progressive reduction of the HR and the ventricular escape rhythm (manifested as markedly lengthened RR intervals at the end of Figure 2A, bottom) ending up with asystole.

R420Q mutation decreased SAN activity in vitro. In order to analyze the intrinsic SAN activity, we dissected the SAN and analyzed the frequency of spontaneous [Ca^{2+}]$_i$ transients by confocal microscopy in SAN cells within the intact tissue (14). Figure 3A shows 2-D confocal images of Fluo-4AM–loaded SAN cells at different times from a WT (upper images) and a KI (lower images) mouse. The cycle length (CL), measured between 2 consecutives spontaneous [Ca^{2+}]$_i$ transients at their maximal upstroke points was significantly longer in KI than in WT cells, evidencing a slower rhythm in RyR$_2$^{R420Q} than in
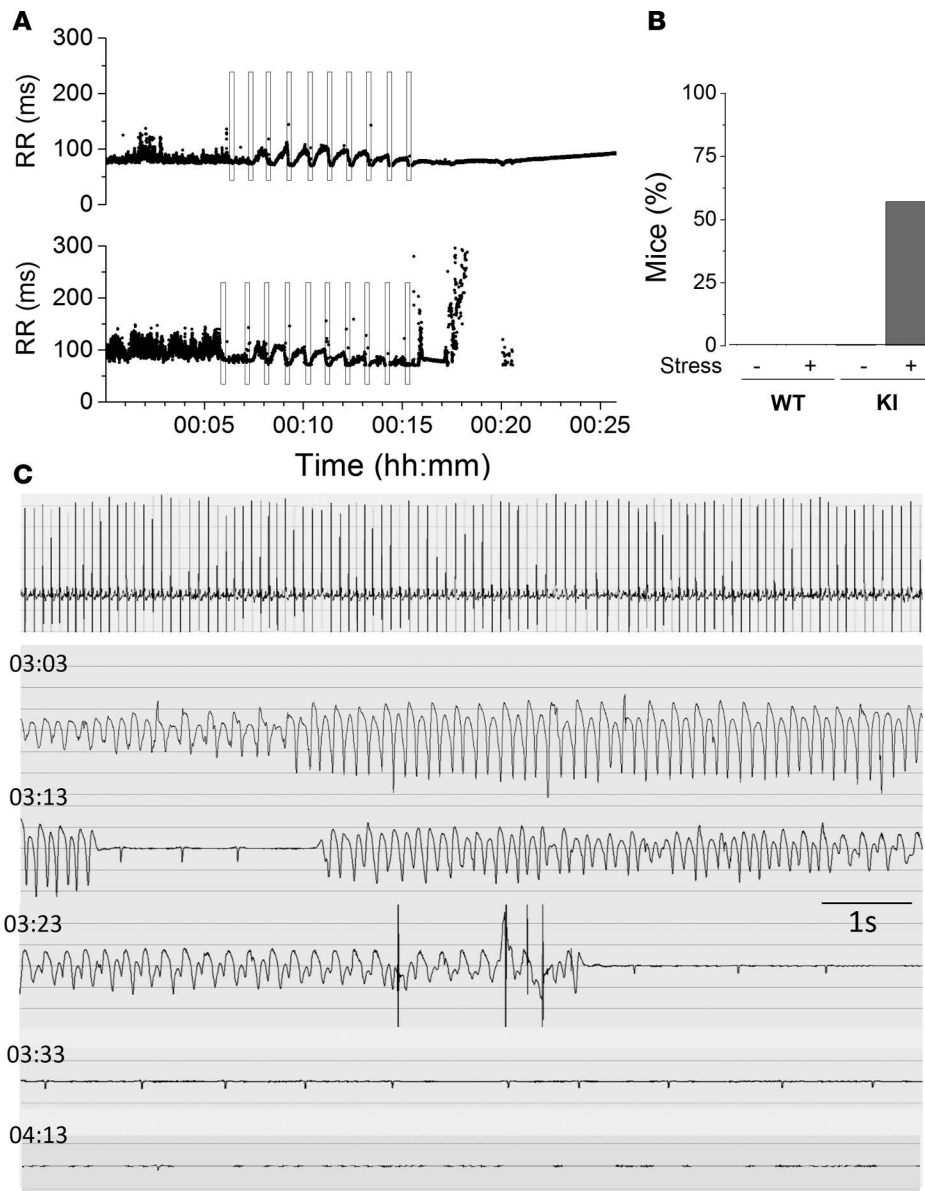
Figure 2. KI mice show SAN dysfunction after emotional stress. (**A**) RR intervals during emotional stress protocol in a WT (top) and a KI (bottom) mouse. Black rectangles represent the 15 s of warm air blowing. Forty-five seconds of rest was allowed before the next air blowing. This experiment was repeated in 8 WT and in 7 KI mice. (**B**) Percentage of mice dead after this protocol in WT and KI mice. (**C**) An example of ECG recorded from a KI mouse, which died after the emotional stress. First line is the ECG during air blowing. Below, ECG 3 hours after the beginning of the protocol (time after the beginning of the protocol on the left). After ventricular tachycardia and a progressively slower ventricular escape rhythm, the mouse died of asystolia. KI, heterozygous for the RyR_2^{R420Q} mutation.

WT SAN (Figure 3B). No difference was found between males and females, so data were pooled. Both male and female KI SAN cells had longer CL than WT, revealing a similar intrinsic defect in KI SAN pacemaker activity both in male and female mice.

Acute ISO treatment decreased the SAN CL in all mice, but the response of KI mice was greater than that of WT (Figure 3C). On the other hand, CCH prolonged the CL equally, regardless of the genotype (Figure 3D). Absolute values are provided in Supplemental Figure 4 and show that, while at basal conditions, RyR_2^{R420Q} SAN beats at slower rate, in the presence of ISO or CCH, both WT and KI SAN beat at similar rate. This is different from our previous data in RyR2[R4496C], where in the presence of ISO CPVT SAN automatic activity remained slower than WT (15).

Membrane clock. Several mechanisms account for the automaticity of pacemaker cells, including the membrane and Ca^{2+} clocks. The membrane clock depends the activity of ion channels located at the sarcolemma, and the Ca^{2+} clock is attributed to the intracellular Ca^{2+} release governed by the RyR_2 channel and the electrogenic Na^+/Ca^{2+} exchanger (NCX) (7, 8), which is also part of the surface membrane electrogenic molecules. Although the difference between KI and WT mice resides in the presence or absence of the RyR_2^{R420Q} mutation, secondary alterations in membrane channel expression could potentially account for the reduction of cell automaticity found in KI SAN. In order to test this possibility, we isolated SAN cells to measure ionic currents with the patch-clamp technique. No difference in current densities was observed in isolated cells from male or female SAN; thus, all data were pooled. Figure 4A shows representative recordings and current-to-voltage relationships of I_f, a key ionic current involved in SAN automaticity (6, 7). As averaged data show, no significant differences were found between groups. Likewise, I_{CaL} in KI mice and WT (Figure 4B) was similar under conditions of Ca^{2+} buffering (presence of 10 mM BAPTA in the pipette solution). However, we observed a reduction in peak I_{CaL} density in KI cells compared with WT cells under control conditions without intracellular Ca^{2+} buffering by BAPTA (Figure 4C). These data suggest that an alteration in intracellular Ca^{2+} dynamics in KI mice induces a decrease in I_{CaL}, which could contribute to the reduction of the SAN pacemaker firing activity.
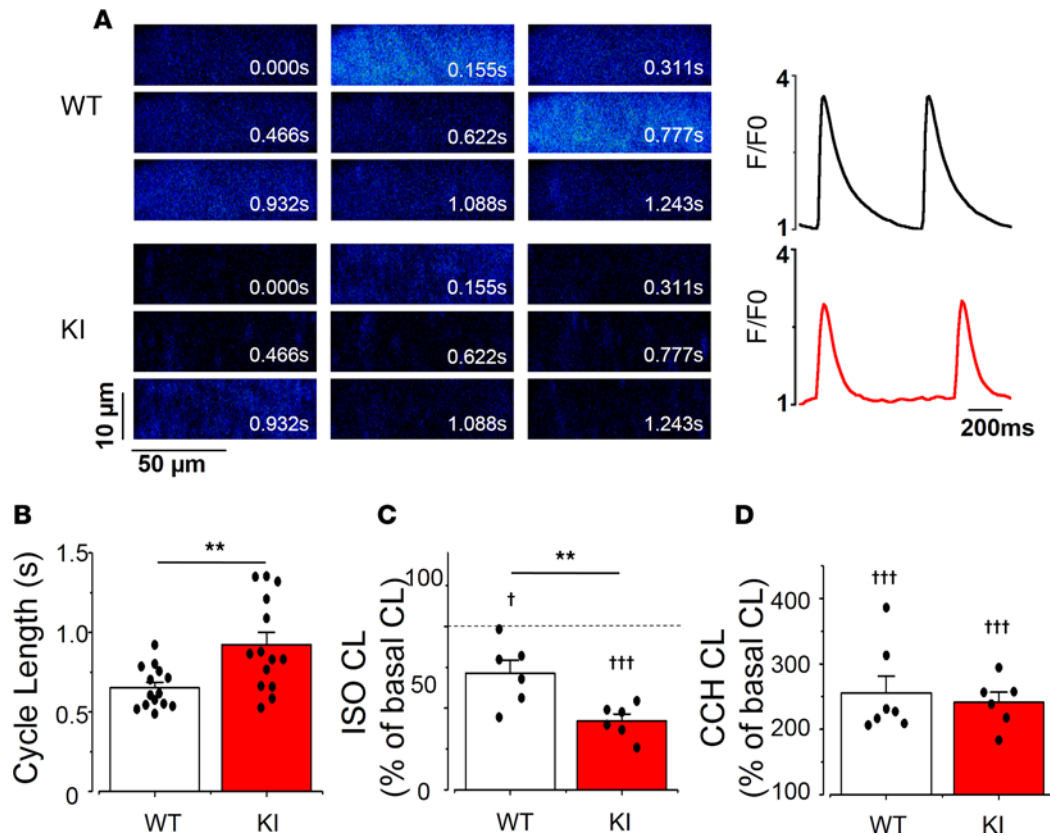
Figure 3. Cycle length (CL) in sinoatrial node (SAN) in KI is longer than in WT. (**A**) Examples of 2-D confocal images (left) of SAN cells within the intact SAN, and the corresponding fluorescence traces (right) in WT (upper) and KI (lower) SAN cell. Fluorescence traces are expressed as F/F_0, where F is the fluorescence signal and F_0 the fluorescence during the diastolic period. (**B**) KI mice have markedly longer cycle lengths (CL; time between two consecutive spontaneous $[Ca^{2+}]_i$ transients) than WT, from $n = 14$ WT and $n = 14$ KI SAN cells. (**C**) Isoproterenol (ISO, 20 nM) decreases SAN CL, although irrespective to the clinical group, as the response in KI SAN ($n = 6$) is larger than in WT ($n = 6$). (**D**) Carbachol (CCH, 500 nM) increases CL in each SAN, and no statistical difference was observed between WT ($n = 7$) and KI ($n = 6$) SAN cells. Each bar displays mean value ± SEM of the node (white for WT and red for KI) with individual data shown on the columns, while each SAN is averaged from several cells (4–13 cells in each SAN). Stars correspond to the comparisons between groups, while crosses show the comparisons inside each group before and after the administration of the drug. $†P < 0.05$; $**P < 0.01$; $†††P < 0.001$ by two (stars) or one (crosses) sample t test. KI, heterozygous for the RyR_2^{R420Q} mutation.

Ca²⁺ clock. We recorded fluorescence Ca²⁺ images of SAN cells within the tissue in the line-scan mode to improve time resolution. Figure 5A shows sample line scan confocal images from one cell of each group. The $[Ca^{2+}]_i$ transient amplitude and the time constant of decay (obtained by fitting the decay fluorescence trace to a single exponential, the duration when the fluorescence extends from the maximum peak to 63% of peak) were similar in KI and WT SAN cells (Figure 5, B and C). However, the $[Ca^{2+}]_i$ transients recorded in KI animals had longer time to peak (Figure 5D). This slowing of the $[Ca^{2+}]_i$ transient upstroke was confirmed by the smaller values on the maximum value of the derivative of the $[Ca^{2+}]_i$ fluorescence trace ($d[F/F_0]/dt$) presented in Figure 5E.

The Ca²⁺ clock model of pacemaking attributes automaticity to spontaneous voltage-independent late diastolic $[Ca^{2+}]_i$ releases (LDCRs) from RyR₂. LDCRs can be seen as "feet" or a "ramp" preceding the $[Ca^{2+}]_i$ transient trace (marked with an arrow in Figure 5F, left). LDCRs activate the sodium-calcium exchanger NCX, which drives the membrane voltage to the threshold of the following action potential (AP), thereby inducing a cell-wide $[Ca^{2+}]_i$ transient caused by opening of L-type Ca²⁺ channels and activation of the Ca²⁺-induced Ca²⁺ release mechanism (7). In agreement with higher RyR_2^{R420Q} open probability, the percentage of recorded cells presenting LDCR was higher in KI SAN cells than in WT SAN counterparts (Figure 5F, right). However, in spite of the increased occurrence of LDCRs, we observed reduced rate of spontaneous $[Ca^{2+}]_i$ transients in KI SAN cells (Figure 3B). We did not consistently record LDCRs in this preparation, probably because of the high degree of synchrony of $[Ca^{2+}]_i$ release among cells in the multicellular preparation. The occurrence of ramp was enhanced by iso application but not modified by CCH (Supplemental Figure 5).
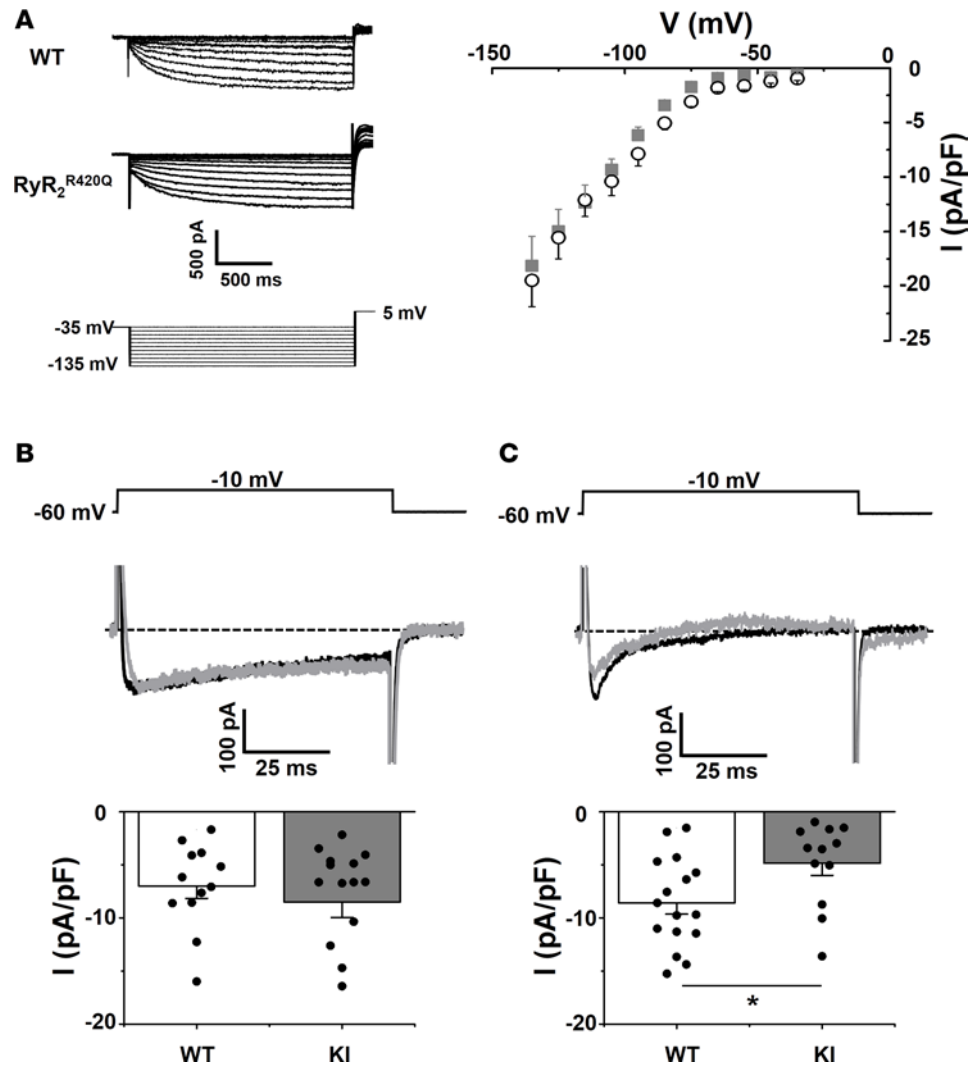
Figure 4. I_f is normal, but I_{CaL} is diminished in KI SAN cells. (**A**) Left, family traces of I_f in a WT (top) and RyR$_2^{R420Q}$ (middle) cell, with the voltage protocol below. Right, I_f current density–voltage relationship in 8 WT cells (open black circles) and 8 KI cells (gray squares). (**B**) I_{CaL} peak current density is unchanged recorded at –10 mV with a 10 mM BAPTA Ca^{2+} buffered intracellular solution, in 12 WT and 15 KI SAN cells. Sample traces at –10 mV and voltage protocol are shown on top. Bar graphs display I_{CaL} averaged current densities (current amplitude divided by the cell capacitance) expressed as the mean ± SEM (white for WT and gray for KI) with individual data shown on the columns. (**C**) I_{CaL} current is decreased at –10 mV in Ca^{2+} unbuffered intracellular solution. Same conditions as in **B**, but without intracellular BAPTA, n = 16 WT and 11 KI cells. *$P < 0.05$ by t test.

Because the amplitude of the spontaneous [Ca^{2+}]$_i$ transient depends on the amount of Ca^{2+} stored in the sarcoplasmic reticulum (SR), we measured the SR Ca^{2+} load by recording the NCX current evoked by rapid caffeine dumping (24). Caffeine application results in opening of all RyR$_2$, which empties SR Ca^{2+} content, and all Ca^{2+} is extruded out of the cell by the electrogenic NCX. Thus, measurement of the NCX current integral is a reliable method to measure the SR Ca^{2+} load. The integral of the caffeine-evoked transient NCX–mediated inward current (Figure 6A) was significantly reduced in the KI SAN cells, indicating a reduced steady state SR Ca^{2+} load in KI SAN cells. The NCX protein expression was similar in SAN from both groups (Figure 6B).

RyR$_2$ expression level. The observed modifications in Ca^{2+} handling of KI SAN might be due to alteration in the RyR$_2$ expression (haploinsufficiency) and/or its phosphorylation status. We evaluated the total RyR$_2$ expression and phosphorylation level by Western blots (examples shown in Figure 6C). Neither the total amount of RyR$_2$, nor their relative phosphorylation at the 2,808 equivalent or at 2,914 equivalent sites, was different among groups (Figure 6, D–F). These data point to an intrinsic defect of the RyR$_2^{R420Q}$ function rather than expression or basal phosphorylation difference.
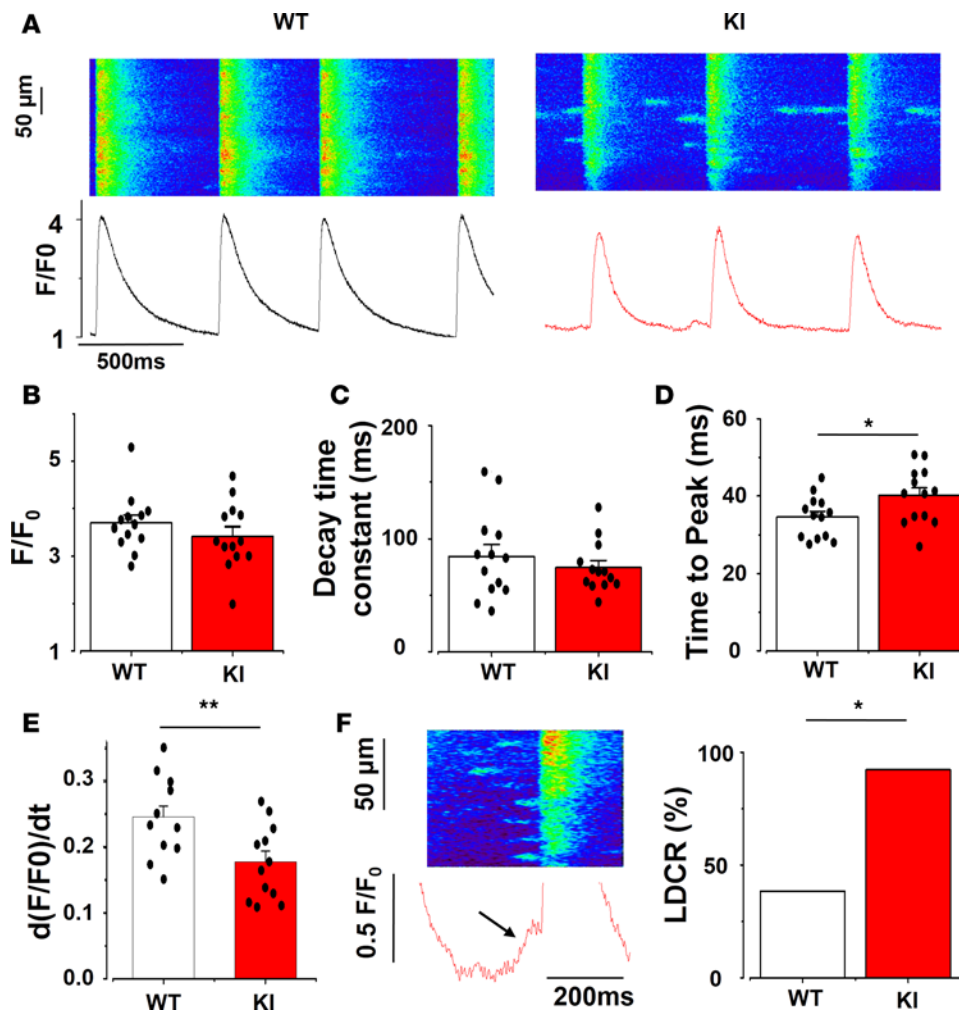
Figure 5. [Ca²⁺]ᵢ transient characteristics in SAN cells. (**A**) Examples of line-scan confocal images showing [Ca²⁺]ᵢ transients (shown as peak, F/F₀, where F is the fluorescence peak and F₀ the fluorescence during the diastolic period) from WT (left) and KI (right) SAN cells. (**B**) [Ca²⁺]ᵢ transient amplitude is unchanged in KI SAN. (**C**) KI SAN cells have similar decay time constant (obtained by fitting the decay portion of the fluorescence trace to a single exponential). (**D**) Time to peak (duration between the beginning of the fluorescence [Ca²⁺]ᵢ transient and its peak) is longer in KI SAN. (**E**) The maximum value of the derivative of the fluorescence [Ca²⁺]ᵢ transient over time is smaller in KI cells, reflecting a slowing of the Ca²⁺ release. (**F**) Example of a ramp (late diastolic Ca²⁺ release, left), and the percentage of cells that present at least one ramp (right), which is higher in KI SAN cells (χ^2). Ramp identification in the fluorescence trace is indicated by the black arrow. Bar graphs display mean value ± SEM of SAN cells with individual data shown on the columns, while each SAN value is averaged from at least 4 cells recorded in the same SAN. WT, white bars, n = 13 SAN cells; KI, red bars, n = 13 SAN cells. *$P < 0.05$, **$P < 0.01$.

Ca²⁺ sparks. Because the presence of the CPVT mutation did not affect either the expression level or the phosphorylation status of the protein, we next examined the RyR₂^{R420Q} function. To this aim, we analyzed Ca²⁺ sparks recorded during the diastolic periods in SAN from WT and KI mice. Figure 7A (left) shows representative examples of confocal images presenting Ca²⁺ sparks in WT and KI SAN cells. Ca²⁺ sparks frequency, which is an estimate of RyR₂ open probability, was globally augmented in KI cells (Figure 7A, right), as in some other CPVT1 models (15, 16, 25). To further examine RyR₂^{R420Q} function, we analyzed Ca²⁺ spark characteristics. Most of them were similar in RyR₂^{R420Q} and WT (amplitude [Figure 7B], Width [Supplemental Figure 6]), except for the longer duration at half-maximum peak of Ca²⁺ sparks (D₅₀, Figure 7C) in RyR₂^{R420Q}-expressing cells. We then went deeper into the Ca²⁺ sparks kinetics. A resonant scanner confocal microscope allowed us to get enough points to measure the time to peak (duration from the beginning of the spark until the maximum peak). Figure 7D shows that the RyR₂^{R420Q} mice presented Ca²⁺ sparks with marked prolongation of the time to peak. In KI cells, there was a shift of the Ca²⁺ spark population to longer time to peak without the appearance of a new population, as it was well fitted to a single normal function (Figure 7D, right). Taken together, the most striking effect of the RyR₂^{R420Q} mutation in Ca²⁺ sparks was a marked prolongation of their duration.
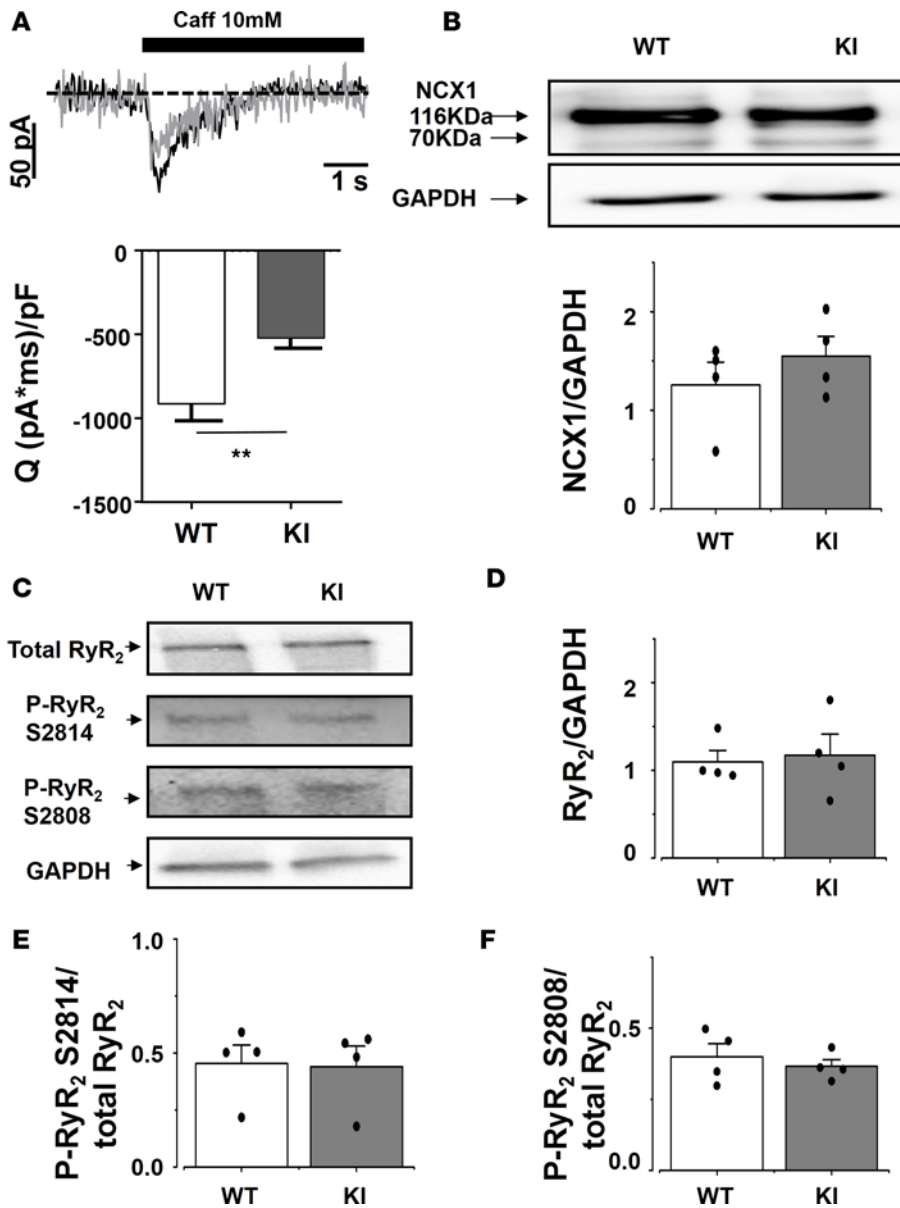
Figure 6. Caffeine-evoked inward current was significantly smaller in KI than in WT SAN cells, without changes in NCX1 or RyR$_2$ protein expression, nor RyR$_2$ phosphorylation level. (**A**) Averaged transient inward current evoked by rapid caffeine application to 17 WT SAN cells and 16 KI cells, with example traces on top. (**B**) NCX expression in dissected SAN is unchanged between KI and WT. WT, $n = 4$ SAN cells, and KI, $n = 4$ SAN cells. (**C**) Examples of blots obtained for total or phosphorylated RyR$_2$ and GAPDH. (**D–F**) Total RyR$_2$ expression (**C**) and phosphorylated (S2814 [**E**] and S2808 [**F**]) RyR$_2$ expressions are unaltered. $n = 4$ SAN cells each. White bars are for WT, and gray bars for KI, representing the mean ± SEM with individual data on the columns. **$*P < 0.01$.
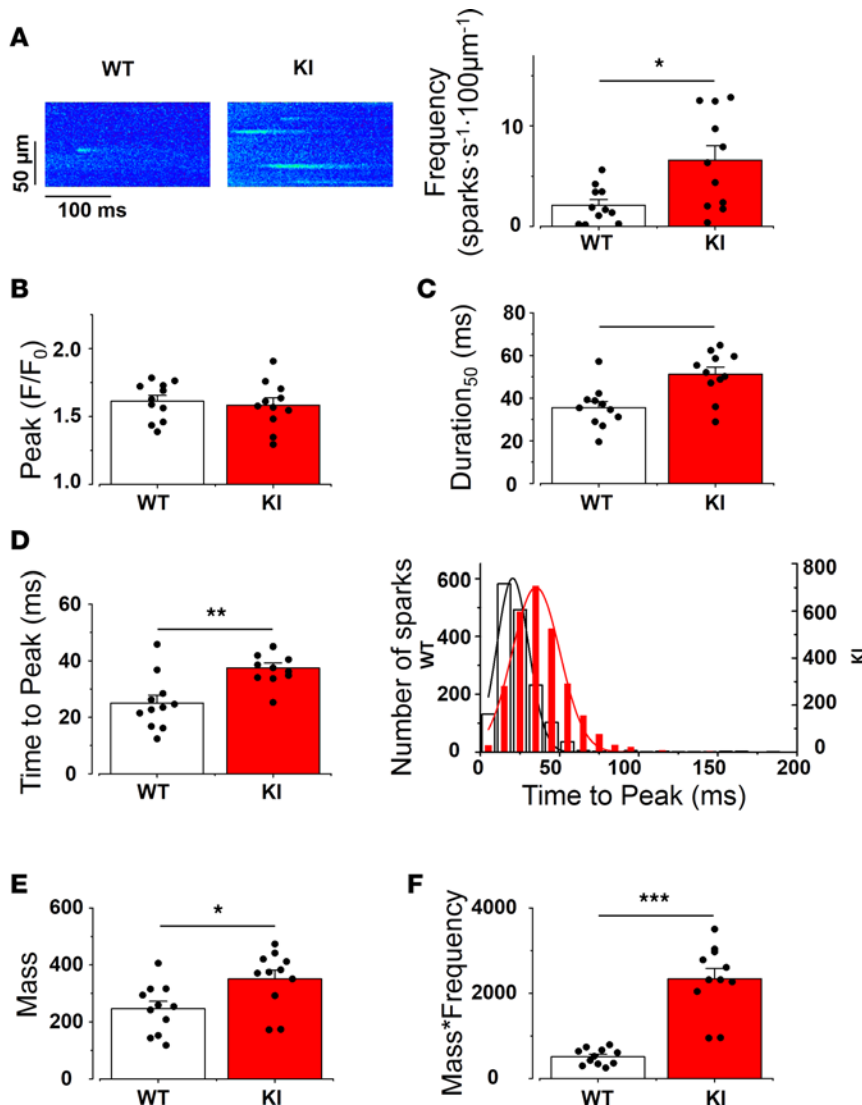
The altered characteristics of Ca^{2+} sparks could modify the total amount of Ca^{2+} released through them. Thus, in order to get insights on the Ca^{2+} leak through Ca^{2+} sparks produced by RyR$_2^{R420Q}$ channels, we calculated Ca^{2+} spark mass by multiplying Ca^{2+} spark characteristics (amplitude × D$_{50}$ × W$_{50}$, Figure 7E) and then by frequency, to obtain a quantitative estimate of the Ca^{2+} released every second, every 100 μm, through Ca^{2+} sparks in each group. Figure 7F shows that SAN cells from KI mice present higher diastolic Ca^{2+} release through Ca^{2+} sparks than WT.

Discussion

Our study uncovers a new arrhythmogenic mechanism in a CPVT mutation located at the N-terminal portion of the channel, the RyR$_2^{R420Q}$. Besides polymorphic ventricular tachycardia upon stress, individuals carrying this mutation, as many other CPVT patients, present with arrhythmias and exhibit slow sinus rates at resting conditions. The presence of RyR$_2^{R420Q}$ produces prolonged Ca^{2+} sparks. This increase in Ca^{2+} leak, instead of accelerating the Ca^{2+} clock, partly inactivates I_{CaL}, disturbing the fine tuning of the coupled clock and resulting in a reduction of the HR. Thus, our data show that an aberrant gain of function of the Ca^{2+} clock inhibits the activity of the voltage clock by inducing a negative Ca^{2+}-to-voltage crosstalk in RyR$_2^{R420Q}$ CPVT SAN cells. This finding highlights the importance of coupled clock mechanisms in the SAN firing rate.

Bradycardia and SAN dysfunction are common in CPVT patients. However, the mechanisms underlying these conditions are still unclear. Besides SAN dysfunction primarily caused by abnormal ion channel activity in SAN cells, there existed the possibility that β-adrenergic signaling could be modified in these patients, as neurons also express RyR$_2$ (26). In fact, patients with arrhythmogenic right ventricular cardiomyopathy, right ventricular outflow tract tachycardia, and ischemic heart disease have been shown to exhibit left ventricular patchy defects in radionuclide distribution, which may identify patients at risk of ventricular arrhythmias and SCD (22). Planar or SPECT imaging with ^{123}I-MIBG is a pharmaceutical suitable test for the presynaptic portion of the cardiac adrenergic innervation (27)— although recently, other techniques have also been used, such as PET with ^{11}C-labeled norepinephrine analog [^{11}C]-hydroxyephedrine (22). A decreased β-AR function has been reported in heart failure, which may also be associated with

Figure 7. KI SAN cells show enhanced Ca²⁺ release through Ca²⁺ sparks. (A) Left, examples of line-scan images of SAN cells within the intact SAN in WT and KI mice. Right, Ca²⁺ spark frequency (number of Ca²⁺ sparks/s/100 μm) recorded from 11 WT and 11 KI SAN cells. At least 4 cells were recorded from each SAN. **(B)** Ca²⁺ spark amplitude (measured as peak F/F₀ as in Figure 5) **(C)** Duration of Ca²⁺ spark at 50% of maximum amplitude is longer in KI SAN cells. **(D)** Time to peak (the duration between the beginning of the spark and the peak) is longer in KI SAN cells. Bar graph on the left shows the averaged value for the SAN cells. On the right, the histogram shows the Ca²⁺ spark time-to-peak distribution (WT: bar bars, KI: red bars from a total of 880 Ca²⁺ sparks in WT and 2,064 Ca²⁺ sparks in KI SAN cells). **(E)** Ca²⁺ spark mass (amplitude × width × duration, indicating the Ca²⁺ release in each spark) is more in KI SAN cells. **(F)** Total Ca²⁺ leak through Ca²⁺ sparks (Ca²⁺ spark mass × frequency, indicating the Ca²⁺ release per second per 100 μm). The bar graph represents the SAN cells mean value ± SEM with individual data on the bar graph. Each value is averaged from all the Ca²⁺ sparks recorded in cells of the same SAN. White bar represents WT, and red bar represents KI. *$P < 0.05$; **$P < 0.01$; ***$P < 0.001$.

SAN dysfunction (28). In this case, SAN failure occurs via a decreased β-AR expression, together with an increase in GRK activity in the heart and mirrored in some cases, in peripheral blood mononuclear cells (28–31), both in humans (28, 29, 32–35) and in experimental models (34–38). A decreased expression and an increased desensitization of β-AR directly led to a loss of β-adrenergic function in the failing heart (28). The data in our CPVT RyR₂^R420Q patients show that altered β-ARs and GRKs expression does not account for sinus bradycardia observed in RyR₂^R420Q mutation carriers. A possible limitation of this conclusion is that, while we obtained expression data in peripheral blood mononuclear cells, all patients included in the study were under treatment with atenolol. However, a lack of information exists as to the specific impact of this β-blocker on β-AR and GRK expression, and it was not ethical to interrupt this treatment once a CPVT diagnosis was confirmed in order to perform the cardiac ¹²³I-MIBG imaging. However, this is the first time that β-AR and GRK expressions have been reported in RyR₂^R420Q patients. Likewise, presynaptic sympathetic innervation grossly evaluated with ¹²³I-MIBG is normal in our CPVT patients and does not account for sinus bradycardia observed in carriers of the RyR2^R420Q mutation. We are aware that a more precise study of regional abnormalities with SPECT technology (currently not available in our center) rather than planar images and on a bigger sample size may be necessary to fully confirm our results. Nevertheless, when evidence obtained by ¹²³I-MIBG is combined with the observation that our RyR₂^R420Q mice responded to β-AR stimulation, we conclude that SAN bradycardia is unlikely to be due to altered β-AR or innervation (Supplemental Figures 1 and 2). While analyzing HR in patients and mice, we confirmed sex-related differences. Adrenergic tone might underlie the observed beating rate differences with respect

to sex, regardless of the mutation presence. Although higher sympathetic activity in men than in women has been suggested (39, 40), women and female mice in general have faster HR, possibly to compensate for their smaller heart size. Our data presented in Figure 1E are reminiscent of this sex difference, with female mice presenting higher HR than male WT mice. Activation of both β-AR and muscarinic receptors in vivo negated all differences in RR intervals between RyR_2^{R420Q} male and female mice (Supplemental Figure 3).

As most CPVT-related mutations concern RyR_2 function, a modification of the Ca^{2+} clock can be expected as a mechanism underlying the slowing of sinus rhythm. We previously analyzed Ca^{2+} handling in cardiac myocytes from the RyR_2^{R4496C} mutation, which is located at the C terminal part of the channel. The defect we identified consisted in enhanced Ca^{2+} sensitivity of the channel (16). Other mechanisms have been invoked in mutations located at other hotspots. In myocytes from KI mice harboring CPVT mutations in the central region (such as the RyR_2^{R2474S}), an altered binding of the mutated RyR_2 to FKBP12.6 (protein that binds RyR_2 and stabilizes it in the closed state) has been identified as the functional mechanism underlying the proarrhythmic behavior of the mutation (41). On the other hand, it has been shown that the zipping-unzipping mechanism (mediated by the N-terminal and central region interaction) was disturbed by the RyR_2^{R2474S} mutation, which induces conformational changes and favors the unzipped state. Although most proposed functional alterations caused by the RyR_2 mutations result in a gain of function, a loss-of-function mutation in the C-terminal portion has been recently reported in a mice model (42).

Herein, we analyzed cells from a mice model harboring the RyR_2^{R420Q} mutation, which we previously identified in a large Spanish family (20). Previously, another mutation in the same residue (R420W) was identified in several CPVT families (43, 44), and besides our two RyR_2^{R420Q} families (ref. 20 and here), two additional reports connect CPVT with the RyR_2^{R420Q} mutation (18, 19). Thus, the 420 site seems to be important for the RyR_2 function. Structural analyses have shown that this residue highly conserved among species plays an important role in the channel conformation (45, 46). The RyR_2^{R420Q} loses the capacity to bind Cl^-, which maintains the three regions of the N terminal domain in place (45), although the functional consequences remained to be elucidated. In a previous study on induced pluripotent cardiac myocytes (iPS-CM), including the RyR_2^{R420Q} mutation, a decrease of spontaneous beating rate was observed, which is consistent with our data (47). However, most of the RyR_2^{R420Q}-expressing cells failed to respond to β-adrenergic stimulation (47), which is different than our data in SAN tissue. The difference might be due to the cardiac cell type, which in our case is adult SAN cardiomyocytes and in iPS-CM are thought to be mostly immature ventricular cardiomyocytes. Here for the first time to our knowledge, we show that the Ca^{2+} sparks in RyR_2^{R420Q} SAN cells are abnormally prolonged, mainly due to a longer time to peak. As the time to peak depends on the open time of the RyR_2, our data are compatible with long openings of the RyR_2^{R420Q} channel. These prolonged Ca^{2+} sparks resulted in increased Ca^{2+} leak and were expected to enhance the Ca^{2+} clock. The Ca^{2+} clock model of pacemaking postulates that a "ramp" of spontaneous RyR_2 dependent Ca^{2+} release during the late diastolic interval activates NCX-mediated inward current (48). In the "coupled clock" model of pacemaking, SAN automaticity is synergistically driven by RyR_2-NCX coupling and the components of the "membrane clock," including I_f and I_{CaL} (7, 49). In the coupled clock model developed to account for rabbit SAN, I_{CaL} activity at each AP cycle keeps appropriate SR Ca^{2+} load so that the Ca^{2+} clock is cyclically reset at the beginning of each diastolic depolarization (7, 49). However, in mouse SAN cells, I_{CaL} contributes to the diastolic depolarization by opening of L-type Cav1.3 channels, possibly initiating the voltage clock together with I_f (8, 50). Moreover, because I_{CaL} drives Ca^{2+} ions in the subsarcolemmal space during the diastolic depolarization, it may contribute to the Ca^{2+} clock. Indeed, we have recently shown that I_{CaL} participates in the activation and synchronization of LDCR by the Ca^{2+}-induced Ca^{2+} release mechanism, probably taking part in the modulation of the Ca^{2+} clock itself (51). Although LDCR are originated as Ca^{2+} sparks, we did a separated analysis of LDCR when they were sufficiently synchronized to build up a ramp just before the global cell $[Ca^{2+}]_i$ transient.

Here we show, for the first time to our knowledge, that Ca^{2+} sparks are more frequent and longer in RyR_2^{R420Q} SAN cells than in WT counterparts, leading to increased diastolic Ca^{2+} release. Although we did not observe the Ca^{2+} ramp in each cell (probably because of the multicellular system we use), the probability of recording such a ramp was higher in RyR_2^{R420Q}-KI than in WT preparations (Figure 5E). Thus, taken together, the higher Ca^{2+} released as Ca^{2+} sparks (Figure 7F) and LDCR indicates enhancement of the Ca^{2+} clock, but the CL remained unexpectedly longer. As shown in Figure 4, although I_{CaL} seems normal when $[Ca^{2+}]_i$ is buffered with BAPTA, it is reduced when $[Ca^{2+}]_i$ is not chelated, reminiscent of the Ca^{2+}-induced inactivation of L-type Ca^{2+} channels. Thus, the boosted Ca^{2+} leak through the RyR_2^{R420Q} partly inactivates I_{CaL}, negatively affecting voltage clock. In addition, Ca^{2+} entry through I_{CaL} also participates in the refilling

of the SR with Ca^{2+} (24). Therefore, in physiological conditions, Ca^{2+}-dependent I_{CaL} inactivation protects from Ca^{2+} overload. Enhanced Ca^{2+} leak in the $RyR2^{R4496C}$ CPVT mutation reduces the I_{CaL} window current, which is the main pathway to refill the cell with Ca^{2+} (52). Here, our data indicate depressed I_{CaL} (Figure 4C and Figure 5D) and a smaller amount of Ca^{2+} stored in the SR (Figure 6A) in KI SAN cells compared with WT. Thus, the aberrant RyR_2^{R420Q} function — although it primarily enhances Ca^{2+} clock — exerts a negative feedback on the voltage clock and also on the Ca^{2+} clock itself.

In summary, we have found a mechanism of SAN bradycardia in a new mice model, to our knowledge, carrying the RyR_2^{R420Q} CPVT mutation. This mutation induces longer channel openings, augmenting the Ca^{2+} leak in each Ca^{2+} spark, negatively affecting the I_{CaL} and SR Ca^{2+} load. Thus, our data show that — while the Ca^{2+} clock is important for the SAN activity — if pathologically exaggerated, it "uncouples" to the coupled clock mechanism, underlining the complexity of the physiological tuning of SAN automaticity.

Methods

Patient characteristics. Adult patients with CPVT were recruited, diagnosed, and treated in Hospital La Fe de Valencia. All patients signed written consent prior to their inclusion in the study. The protocols (clinical assessment, treatment, and biochemical assays) were approved by the Ethics Committee of the Hospital La Fe, University of Valencia, and conducted in accordance with the Declaration of Helsinki.

HR. HR from each member of the Spanish family previously reported by our group (19), and the second apparently unrelated family with the RyR_2^{R420Q} mutation, was obtained from a resting 12-lead ECG register. Only data before any β-blocker treatment were considered. We excluded two babies (3 and 24 months at the time of the recording) and 4 brothers who were marathon runners.

GRK and β-AR quantification. Eight adult CPVT patients (2 males and 6 females) and 6 controls (healthy volunteers similar to patients with respect to sex and age and with no personal or family history of heart diseases, effort-related syncopes, or SCD) were included.

All patients and none of the controls were on β-blockers (atenolol) at the time of the blood sampling. Blood samples (10 ml) were obtained in the morning, after a minimum of 8 hours of fasting, and were anticoagulated with EDTA. Blood samples were treated as previously described (31) using Lymphoprep (STEMCELL Technologies or Progen Biotechnik or AXIS-SHIELD Density Gradient Media) to isolate the peripheral blood mononuclear cells following the manufacture's conditions. To perform the quantitative PCR (qPCR), total RNA was obtained as previously described (53) and was quantified and analyzed by running 1 μg of each sample by microfluidic electrophoresis using the Experion automated electrophoresis system (Bio-Rad) following the manufacture's conditions. cDNA synthesis was carried out with 500 ng of total RNA and 250 ng of oligo(dT) as a primer at 70°C in diethyl pyrocarbonate–treated (DEPC-treated) water. The reactant (20 μl) contained ImProm-II TM reaction buffer, 3 mM MgCl2, 20 U of Recombinant RNAsin Ribonuclease Inhibitor (Promega), 0.5 mM of each deoxynucleoside triphosphate, and 1 μl of ImProm-II TM Reverse Transcriptase (Promega). This was incubated at 25°C for 5 minutes (annealing step), followed by an extension step at 42°C for 60 minutes and a final step at 70°C for 15 minutes (heat-inactivate). The mRNAs encoding the $β_1$ and $β_2$ adrenoceptors, the 3 GRKs mainly expressed in lymphocytes (GRK2, GRK3, and GRK5) and *GAPDH* as internal standard, were quantified by TaqMan real-time RT-PCR with a GeneAmp 7500 Fast System (Applied Biosystems). We analyzed (in duplicate reactions) a 10-fold dilution of the RT reaction of each sample using the TaqMan Gene Expression Assays (Applied Biosystems). The specific primer-probes were: $β_1$-AR, Hs00265096_s1; $β_2$-AR, Hs00240532_s1; GRK2, Hs00176395_m1; GRK3, Hs00178266_m1; GRK5, Hs00178389_m1; and *GAPDH,* Hs99999905_m1 (Applied Biosystems). Real-time PCR reactions were done in 25 μl with TaqMan Universal PCR Master Mix (Applied Biosystems), including 5 μl of diluted RT reaction and 1.25 μl of 20× TaqMan Gene Expression Assay Mix (250 nmol/l for the probe and 900 nmol/l for each primer). cDNA was amplified following the manufacture's conditions: one initial hold-step at 95°C for 10 minutes, a second step with 40 cycles, 15 seconds at 95°C (denaturation), and 1 minute at 60°C (annealing/extension). The targets and reference (*GAPDH*) were amplified in parallel reactions. The Ct values obtained for each gene were referenced to *GAPDH* and converted into the linear form using the term $2^{-\Delta Ct}$ as a value directly proportional to the mRNA copy number.

Cardiac sympathetic imaging. Two male and 6 female adult CPVT patients underwent ^{123}I-MIBG imaging to assess the presynaptic reuptake of norepinephrine. No controls were enrolled, since this test exposes the patients to ionizing radiation (although minimal) and reference normal images are well known. Twenty minutes before the test, patients were pretreated with 400 mg oral potassium perchlorate to block the uptake

of free iodine-123 by the thyroid gland. Then, 370 MBq ^{123}I-MIBG (Adreview, General Electric Healthcare) at rest was i.v. administered. Planar imaging was acquired from an anterior thoracic view 10 minutes and 4 hours after tracer administration, using a dual-head camera system (Philips BrightView), equipped with parallel-hole, low energy, high-resolution collimators. A 256 × 256 matrix was used, and 20% energy peak was centered on the 159 KeV (±10%) energy peak of ^{123}I-MIBG. Early and late H/M ratios and WR were calculated using planar images, derived by manually drawing separate regions of interest around the entire heart and upper mediastinum, and measuring counts per pixel within these regions.

KI mice. RyR2[R420Q] mice were created by PHENOMIN, Institut Clinique de la Souris (ICS), CNRS, INSERM, University of Strasbourg, France http://www.phenomin.fr/. Mutation converted the arginine residue at amino acid 420 to glutamine.

Experiments were performed on male and female heterozygous RyR_2[R420Q] mice and their WT littermates (aged about 6 months) in accordance with the ethics principles laid down by the French Ministry of Agriculture and European Economic Community (ECC) directive 86/609/ECC.

In vivo telemetric ECG recording. To monitor ECGs in awake, free-moving mice, the transmitters (7 ETA-F10) were implanted s.c. to the mice. The negative lead was placed on the upper right chest, and the positive lead was placed on the left abdomen below the left diaphragm and below the heart. During the s.c. implantation of ECG transmitter, the mouse was placed on a warm pad (37°C). Anesthesia was induced with an Isoflurane (2.5%) inhalation apparatus (MINERVE Equipement veterinaire; catalog 0901128) for anesthesia induction. During surgery, the animal was continuously receiving isofluorane (1.5%). At least 7 days after surgery, ECGs were recorded in resting conditions and 5 minutes after epinephrine/caffeine (2/120 mg/kg, i.p.) or ISO (1 mg/kg, i.p.) challenge. Data were collected with a signal transmitter receiver (Data Sciences International) connected to a data acquisition system and analyzed with ECG auto software (EMKA Technologies).

In vitro intact SAN cell recording. Mice were anesthetized by sodium pentobarbital (50 mg/kg, i.p.). The hearts were quickly removed from the animal and placed in Tyrode solution (NaCl 140 mM, KCl 5.4 mM, $CaCl_2$ 1.8 mM, $MgCl_2$ 1 mM, HEPES 5 mM, and glucose 5.5 mM, pH 7.4, titrated with NaOH). The solution was oxygenated to saturation and maintained at 37°C. SAN and some surrounding atrial tissue were dissected and pinned down with the endocardial side up in homemade optical chambers bathed with Tyrode solution as previously described (15). The tissue was loaded with fluo-4 AM (Invitrogen) (30 μM) during 60 minutes at 37°C. Images were recorded with a resonant scanning confocal microscope Leica SP5, equipped with a white laser fitted to 500 nm. Excitation was collected at > 510 nm. Two-dimensional and XT images were recorded from the primary pacemaker region. Experiments and recordings were performed at 37°C. Analysis was made in IDL software (Exelis Visual Inc.) by homemade routines.

Western blot. SAN dissected from WT and KI mice were lysed by Bertin homogenizer with RIPA lysis buffer, run on 4%–20% discontinuous gradient polyacrylamide gels, and transferred to PVDF membranes. PVDF membranes were incubated with blocking buffer of TBS with Tween-20 (1%) and nonfat dry milk (5%). Membranes were then incubated with primary antibodies diluted in 5% milk TBS overnight at 4°C, followed by the secondary antibodies. NCX1 (Swant, R3F1), RyR_2 (Thermo Fisher Scientific, MA3-916), S2814 phosphorylated RyR2 (Badrilla, A010-31AP), S2808 phosphorylated RyR_2 (Badrilla, A010-30AP), and GAPDH (Abcam) primary antibodies were used. HCN4 primary antibody was a sample from Alomone Labs (APC-052). Antigen complexes were visualized with ChemiDoc and quantified with Image J (NIH).

Isolation of sinoatrial node myocytes. SAN myocytes were isolated from WT and RyR2[R420Q]-KI mice as previously described (54). Briefly, mice were anesthetized using 0.01 mg/g xylazine (2% Rompun; Bayer AG) and 0.1 mg/g ketamine (Imalgene; Merial Laboratories), and beating hearts were quickly removed.

The SAN regions were excised in prewarmed (35 °C) Tyrode's solution. SAN tissue strips were then transferred into a "low-Ca^{2+}–low-Mg^{2+}" solution containing (in mM/l) 140 NaCl, 5.4 KCl, 0.5 $MgCl_2$, 0.2 $CaCl_2$, 1.2 KH_2PO_4, 50 taurine, and 5.5 D-glucose; 1 mg/ml BSA; and 5 HEPES-NaOH, adjusted to pH 6.9 with NaOH. Tissue was digested by Liberase TH (229 U/mL; Roche Diagnostics), elastase (1.9 U/ml; Boehringer Mannheim), and 200 μM $CaCl_2$. Digestion was carried out for 9–13 minutes at 35 °C, under manual mechanical agitation. Tissue strips were then washed and transferred into a modified Kraftbrühe (KB) medium containing (in mM/l) 70 L-glutamic acid, 20 KCl, 80 KOH, 10 (±)D-β-OH-butyric acid, 10 KH_2PO_4, and 10 taurine; 1 mg/ml BSA; and 10 Hepes-KOH, adjusted to pH 7.4 with KOH. Single SAN myocytes were then isolated by agitation in KB solution at 35 °C. Cellular automaticity was restored by readapting the cells to a physiological extracellular Ca^{2+}concentration by addition

of a solution containing (in mM/l) 10 NaCl, 1.8 CaCl$_2$, and normal Tyrode's solution containing BSA (1 mg/ml). The final cell storage solution contained (in mM/l) 100 NaCl, 35 KCl, 1.3 CaCl$_2$, 0.7 MgCl$_2$, 14 L-glutamic acid, 2 (±)D-β-OH-butyric acid, 2 KH$_2$PO$_4$, and 2 taurine; and 1 mg/ml BSA (pH 7.4).

Patch-clamp recordings of SAN myocytes. The extracellular Tyrode's solution used in all recordings contained (in mM): 140.0 NaCl, 5.4 KCl, 1.8 CaCl$_2$, 1.0 MgCl$_2$, 5.0 HEPES-NaOH, and 5.5 d-glucose (adjusted to pH 7.4 with NaOH).

I_f and I_{CaL} were recorded under standard whole-cell configuration. Patch-clamp electrodes had a resistance of 4–5 MΩ when filled with an intracellular solution containing (in mM): K$^+$-aspartate 130, NaCl 10.0, ATP-Na$^+$ salt 2.0, creatine phosphate 6.6, GTP-Mg^{2+} 0.1, CaCl$_2$ 0.04 (pCa 7.0), and HEPES-KOH 10.0 (adjusted to pH 7.2 with KOH). I_f was recorded from a holding potential (HP) of –35 mV by 2 seconds lasting hyperpolarizing steps from –35 to –135 mV in 10-mV increment steps. To properly quantify I_f current densities, 2 mM BaCl$_2$ was added to standard Tyrode to block I$_{K1}$. For I_{CaL} recording, 30 μM tetrodotoxin (TTX, Latoxan) to block I_{Na} and 10 mmol/L BAPTA was added in the pipette solution when requested by the protocol. I_{CaL} was recorded from a HP of –60 mV to inactivate $I_{Ca,T}$ (50). Current was evoked at depolarizing voltage by applying 100 ms lasting steps from –55 to +20 mV in 5 mV– or 10 mV–step increments.

The inward current evoked by rapid application (spritz) of caffeine 10 mM was measured at HP of –45 mV. All currents were recorded using an Axopatch 700B amplifier (Molecular Devices), acquired with Clampex (pClamp9; Molecular Devices), and analyzed with Prism 6 software (GraphPad software). Signals were sampled at 10 kHz and low-pass filtered at 5 kHz. The recording temperature was set to 36°C. All chemicals were from Sigma-Aldrich.

Statistics. Two-way ANOVA was used for multiple comparisons. An unpaired *t* test was used to compare 2 independent groups. A paired *t* test was used to compare measurements made in the same mice or in the same cells under 2 different conditions. The *t* tests were two-tailed and a value of *P* < 0.05 was considered significant. Results are expressed as mean ± SEM. The Graph Pad Prism 4 Software and the Origin 9 (Microcal) software were used.

Study approval. Animal study was approved by the French Ministry (Ministère de l'Éducation Nationale, de l'Enseignement supérieur et de la Recherche) no. B9201901. The human protocol was approved by the Ethics Committee of the Hospital La Fe, University of Valencia, and conducted in accordance with the Declaration of Helsinki. Written consent was given by the patients and controls prior to the inclusion in this study.

Author contributions

YYW did all the in vitro confocal experiments and analyses, telemetry implants surgery, and genotyping; some of the in vivo recordings and analyses; and manuscript preparation. PM did the patch-clamp experiments and analysis, and edited the manuscript. EMS did the ECG arrhythmia analysis. AZ did the firsts ECGs implants surgery, recording, and analysis. OV did some ECG recording and analyses. EZ designed the part of the study regarding the insights on the sympathic innervation, participated collecting clinical data and obtaining the biological samples from patients, supervised arrhythmia analysis, and edited the manuscript. PD performed and evaluated the β-AR and GRK analyses. CR performed and evaluated the ^{123}I-MIBG cardiac imaging. DD participated collecting clinical data and obtaining the biological samples from patients. MEM supervised the patch-clamp experiments and edited the manuscript. JPB supervised most of the work and edited the manuscript. AMG supervised the work, wrote the IDL programs for analyses of confocal images, helped with analyses, and wrote the manuscript.

Acknowledgments

Address correspondence to: Ana María Gómez or Jean-Pierre Benitah, Faculté de Pharmacie, Université Paris Sud, 5 Rue Jean Baptiste Clément, 92296 Châtenay-Malabry, France. Phone: 33.146.83.57.18; E-mail: ana-maria.gomez@inserm.fr (A.M. Gómez); jean-pierre.benitah@inserm.fr (J.P. Benitah). Or to: Matteo Mangoni, Institut de Génomique Fonctionnelle, 141, rue de la Cardonille, 34094 Montpellier, France. Phone: 33.4.99.61.99.69; E-mail: Matteo.Mangoni@igf.cnrs.fr. Or to: Esther Zorio, Servicio de Cardiología, Hospital Universitario y Politécnico La Fe, Avinguda de Fernando Abril Martorell, 106, 46026 Valencia, Spain. Phone: 34.9.61.24.58.49; E-mail: zorio_est@gva.es.

AZ's present address is: Institute of Molecular Physiology and Genetics, Slovak Academy of Sciences, Bratislava, Slovakia.

1. Leenhardt A, Lucet V, Denjoy I, Grau F, Ngoc DD, Coumel P. Catecholaminergic polymorphic ventricular tachycardia in children. A 7-year follow-up of 21 patients. *Circulation*. 1995;91(5):1512–1519.
2. Postma AV, et al. Catecholaminergic polymorphic ventricular tachycardia: RYR2 mutations, bradycardia, and follow up of the patients. *J Med Genet*. 2005;42(11):863–870.
3. Sumitomo N, et al. Association of atrial arrhythmia and sinus node dysfunction in patients with catecholaminergic polymorphic ventricular tachycardia. *Circ J*. 2007;71(10):1606–1609.
4. Domingo D, López-Vilella R, Arnau MÁ, Cano Ó, Fernández-Pons E, Zorio E. A new mutation in the ryanodine receptor 2 gene (RYR2 C2277R) as a cause catecholaminergic polymorphic ventricular tachycardia. *Rev Esp Cardiol (Engl Ed)*. 2015;68(1):71–73.
5. van der Werf C, et al. Flecainide therapy reduces exercise-induced ventricular arrhythmias in patients with catecholaminergic polymorphic ventricular tachycardia. *J Am Coll Cardiol*. 2011;57(22):2244–2254.
6. DiFrancesco D. The role of the funny current in pacemaker activity. *Circ Res*. 2010;106(3):434–446.
7. Lakatta EG, Maltsev VA, Vinogradova TM. A coupled SYSTEM of intracellular Ca2+ clocks and surface membrane voltage clocks controls the timekeeping mechanism of the heart's pacemaker. *Circ Res*. 2010;106(4):659–673.
8. Mangoni ME, Nargeot J. Genesis and regulation of the heart automaticity. *Physiol Rev*. 2008;88(3):919–982.
9. Rubenstein DS, Lipsius SL. Mechanisms of automaticity in subsidiary pacemakers from cat right atrium. *Circ Res*. 1989;64(4):648–657.
10. Rigg L, Terrar DA. Possible role of calcium release from the sarcoplasmic reticulum in pacemaking in guinea-pig sino-atrial node. *Exp Physiol*. 1996;81(5):877–880.
11. Rigg L, Heath BM, Cui Y, Terrar DA. Localisation and functional significance of ryanodine receptors during beta-adrenoceptor stimulation in the guinea-pig sino-atrial node. *Cardiovasc Res*. 2000;48(2):254–264.
12. Lyashkov AE, et al. Calcium cycling protein density and functional importance to automaticity of isolated sinoatrial nodal cells are independent of cell size. *Circ Res*. 2007;100(12):1723–1731.
13. Maltsev VA, Yaniv Y, Maltsev AV, Stern MD, Lakatta EG. Modern perspectives on numerical modeling of cardiac pacemaker cell. *J Pharmacol Sci*. 2014;125(1):6–38.
14. Bround MJ, et al. Cardiac ryanodine receptors control heart rate and rhythmicity in adult mice. *Cardiovasc Res*. 2012;96(3):372–380.
15. Neco P, et al. Paradoxical effect of increased diastolic Ca2+ release and decreased sinoatrial node activity in a mouse model of catecholaminergic polymorphic ventricular tachycardia. *Circulation*. 2012;126(4):392–401.
16. Fernández-Velasco M, et al. Increased Ca2+ sensitivity of the ryanodine receptor mutant RyR2R4496C underlies catecholaminergic polymorphic ventricular tachycardia. *Circ Res*. 2009;104(2):201–209.
17. Zissimopoulos S, Lai FA. Ryanodine receptor structure, function and pathophysiology. In: Krebs J, Michalak M, eds. *Calcium: A Matter of Life or Death*. Amsterdam, Netherlands: Elsevier Science; 2007:287–344.
18. Medeiros-Domingo A, et al. The RYR2-encoded ryanodine receptor/calcium release channel in patients diagnosed previously with either catecholaminergic polymorphic ventricular tachycardia or genotype negative, exercise-induced long QT syndrome: a comprehensive open reading frame mutational analysis. *J Am Coll Cardiol*. 2009;54(22):2065–2074.
19. Arad M, Glikson M, El-Ani D, Monserrat-Inglesias L. A family with recurrent sudden death and no clinical clue. *Ann Noninvasive Electrocardiol*. 2012;17(4):387–393.
20. Domingo D, et al. Non-ventricular, Clinical, and Functional Features of the RyR2(R420Q) Mutation Causing Catecholaminergic Polymorphic Ventricular Tachycardia. *Rev Esp Cardiol (Engl Ed)*. 2015;68(5):398–407.
21. Priori SG, et al. Clinical and molecular characterization of patients with catecholaminergic polymorphic ventricular tachycardia. *Circulation*. 2002;106(1):69–74.
22. Travin MI, Feng D, Taub CC. Novel Imaging Approaches for Predicting Arrhythmic Risk. *Circ Cardiovasc Imaging*. 2015;8(11):e003019.
23. Knollmann BC, et al. Familial hypertrophic cardiomyopathy-linked mutant troponin T causes stress-induced ventricular tachy-

cardia and Ca2+-dependent action potential remodeling. *Circ Res*. 2003;92(4):428–436.

24. Trafford AW, Díaz ME, Eisner DA. Coordinated control of cell Ca(2+) loading and triggered release from the sarcoplasmic reticulum underlies the rapid inotropic response to increased L-type Ca(2+) current. *Circ Res*. 2001;88(2):195–201.

25. Fernández-Velasco M, et al. RyRCa2+ leak limits cardiac Ca2+ window current overcoming the tonic effect of calmodulinin mice. *PLoS One*. 2011;6(6):e20863.

26. Berridge MJ. Neuronal calcium signaling. *Neuron*. 1998;21(1):13–26.

27. Teresińska A. Metaiodobenzylguanidine scintigraphy of cardiac sympathetic innervation. *Nucl Med Rev Cent East Eur*. 2012;15(1):61–70.

28. Iaccarino G, et al. Elevated myocardial and lymphocyte GRK2 expression and activity in human heart failure. *Eur Heart J*. 2005;26(17):1752–1758.

29. Brodde OE, Kretsch R, Ikezono K, Zerkowski HR, Reidemeister JC. Human beta-adrenoceptors: relation of myocardial and lymphocyte beta-adrenoceptor density. *Science*. 1986;231(4745):1584–1585.

30. Hata JA, et al. Lymphocyte levels of GRK2 (betaARK1) mirror changes in the LVAD-supported failing human heart: lower GRK2 associated with improved beta-adrenergic signaling after mechanical unloading. *J Card Fail*. 2006;12(5):360–368.

31. Oliver E, et al. beta-Adrenoceptor and GRK3 expression in human lymphocytes is related to blood pressure and urinary albumin excretion. *J Hypertens*. 2010;28(6):1281–1289.

32. Bristow MR, et al. Reduced beta 1 receptor messenger RNA abundance in the failing human heart. *J Clin Invest*. 1993;92(6):2737–2745.

33. Ungerer M, et al. Expression of beta-arrestins and beta-adrenergic receptor kinases in the failing human heart. *Circ Res*. 1994;74(2):206–213.

34. Ungerer M, Kessebohm K, Kronsbein K, Lohse MJ, Richardt G. Activation of beta-adrenergic receptor kinase during myocardial ischemia. *Circ Res*. 1996;79(3):455–460.

35. Montó F, et al. β2- and β1-Adrenoceptor Expression Exhibits a Common Regulatory Pattern With GRK2 and GRK5 in Human and Animal Models of Cardiovascular Diseases. *J Cardiovasc Pharmacol*. 2015;66(5):478–486.

36. Rockman HA, et al. Expression of a beta-adrenergic receptor kinase 1 inhibitor prevents the development of myocardial failure in gene-targeted mice. *Proc Natl Acad Sci USA*. 1998;95(12):7000–7005.

37. Iaccarino G, et al. Regulation of myocardial betaARK1 expression in catecholamine-induced cardiac hypertrophy in transgenic mice overexpressing alpha1B-adrenergic receptors. *J Am Coll Cardiol*. 2001;38(2):534–540.

38. Sato PY, Chuprun JK, Schwartz M, Koch WJ. The evolving impact of g protein-coupled receptor kinases in cardiac health and disease. *Physiol Rev*. 2015;95(2):377–404.

39. Britton A, Shipley M, Malik M, Hnatkova K, Hemingway H, Marmot M. Changes in heart rate and heart rate variability over time in middle-aged men and women in the general population (from the Whitehall II Cohort Study). *Am J Cardiol*. 2007;100(3):524–527.

40. Dart AM, Du XJ, Kingwell BA. Gender, sex hormones and autonomic nervous control of the cardiovascular system. *Cardiovasc Res*. 2002;53(3):678–687.

41. Lehnart SE, et al. Leaky Ca2+ release channel/ryanodine receptor 2 causes seizures and sudden cardiac death in mice. *J Clin Invest*. 2008;118(6):2230–2245.

42. Zhao YT, et al. Arrhythmogenesis in a catecholaminergic polymorphic ventricular tachycardia mutation that depresses ryanodine receptor function. *Proc Natl Acad Sci USA*. 2015;112(13):E1669–E1677.

43. Nishio H, Iwata M, Suzuki K. Postmortem molecular screening for cardiac ryanodine receptor type 2 mutations in sudden unexplained death: R420W mutated case with characteristics of status thymico-lymphaticus. *Circ J*. 2006;70(11):1402–1406.

44. Bauce B, et al. Screening for ryanodine receptor type 2 mutations in families with effort-induced polymorphic ventricular arrhythmias and sudden death: early diagnosis of asymptomatic carriers. *J Am Coll Cardiol*. 2002;40(2):341–349.

45. Kimlicka L, Tung CC, Carlsson AC, Lobo PA, Yuchi Z, Van Petegem F. The cardiac ryanodine receptor N-terminal region contains an anion binding site that is targeted by disease mutations. *Structure*. 2013;21(8):1440–1449.

46. Borko L, et al. Structural insights into the human RyR2 N-terminal region involved in cardiac arrhythmias. *Acta Crystallogr D Biol Crystallogr*. 2014;70(Pt 11):2897–2912.

47. Novak A, et al. Cardiomyocytes generated from CPVTD307H patients are arrhythmogenic in response to β-adrenergic stimulation. *J Cell Mol Med*. 2012;16(3):468–482.

48. Vinogradova TM, Bogdanov KY, Lakatta EG. beta-Adrenergic stimulation modulates ryanodine receptor Ca(2+) release during diastolic depolarization to accelerate pacemaker activity in rabbit sinoatrial nodal cells. *Circ Res*. 2002;90(1):73–79.

49. Yaniv Y, Lakatta EG, Maltsev VA. From two competing oscillators to one coupled-clock pacemaker cell system. *Front Physiol*. 2015;6:28.

50. Mangoni ME, et al. Functional role of L-type Cav1.3 Ca2+ channels in cardiac pacemaker activity. *Proc Natl Acad Sci USA*. 2003;100(9):5543–5548.

51. Torrente AG, et al. L-type Cav1.3 channels regulate ryanodine receptor-dependent Ca2+ release during sino-atrial node pacemaker activity. *Cardiovasc Res*. 2016;109(3):451–461.

52. Fernández-Velasco M, et al. RyRCa2+ leak limits cardiac Ca2+ window current overcoming the tonic effect of calmodulinin mice. *PLoS One*. 2011;6(6):e20863.

53. Montó F, et al. Different expression of adrenoceptors and GRKs in the human myocardium depends on heart failure etiology and correlates to clinical variables. *Am J Physiol Heart Circ Physiol*. 2012;303(3):H368–H376.

54. Mangoni ME, Nargeot J. Properties of the hyperpolarization-activated current (I(f)) in isolated mouse sino-atrial cells. *Cardiovasc Res*. 2001;52(1):51–64.